REMARKS

Favorable reconsideration is respectfully requested in view of the foregoing amendments and the following remarks.

I. CLAIM STATUS AND AMENDMENTS

Claims 11-22 were pending in this application when last examined and stand rejected.

Claim 11 is amended to clarify the claimed invention. Support can be found on page 11, lines 20-24 and Figure 1 of the specification as filed.

Claim 21 is amended to correct a typographical error.

The paragraph on page 12, line 28 to page 13, line 20 of the specification has been amended to clarify the language and to correct an obvious grammatical error.

No new matter has been added.

II. FOREIGN PRIORITY

Enclosed is a certified copy of JP 2002-337212 (Attachment A). A verified English translation of JP 2002-337212 (Attachment B) is also submitted herewith.

Applicants note that the claim for Foreign Priority has now been perfected and request acknowledgement of such in the next Office Action.

III. OBJECTIONS

On page 3 of the Office Action, claims 21 and 11 were objected to for the noted reasons. Claim 21 is amended and therefore overcomes the noted rejection. It is further noted that claim 11 has been clarified to indicate that both substitutions are required. Thus, these objections are overcome.

IV. UTILITY/ENABLEMENT/WRITTEN DESCRIPTION REJECTIONS

On pages 3-5, claims 11-22 were rejected under 35 U.S.C. § 101 for lack of either a specific and substantial asserted utility or a well established utility.

On page 5, claims 11-22 were rejected under 35 U.S.C. § 112, first paragraph, for not having a specific and substantial asserted utility or a well established utility.

Finally, on pages 5-8, claims 11-22 were rejected under 35 U.S.C. § 112, first paragraph, for failing to comply with the written description requirement.

These rejections are addressed together as they both flow from the Office's contention that the claimed invention does not have a substantial or well-established utility.

Applicants respectfully traverse these rejections as applied to the amended claims.

Attached herewith are references by Liu et al. (Attachment C) and Soong et al. (Attachment D) indicating that nanomotors show promise as mechanical components in hybrid nano-engineered systems. Further, it is noted that page 1 and 2 of the specification indicate that nanomotors are required for fabrication of nanomachines. Further, nanomotors are required for the process of micromachining and nanomachining to create such nanomachines.

Applicants submit that these are credible uses for the nanomachines of the present invention and such claimed nanomotors can be envisioned to be used in any system that requires extremely miniaturized motors or actuators. Applicants further note that the Office appears to be misapplying the utility requirement as such requirement requires a credible use to a person of skill in the art but does not require the demonstration of an actual use. Finally, Applicants note that motors have a well-established utility, no matter how small the motor is.

In regard to the rejection of claim 11 on page 7, it is noted claim 11 is amended to clarify the claimed invention and therefore this concern is overcome.

In regard to claim 12, it is noted that "substrate" is discussed on page 12, lines 18-26. It is obvious to a person of skill in the art that the substrate of claim 12 is a support so that it is "possible to efficiently transmit the rotation of the D subunit".

Finally, with regard to the limitation "joint material" in claims 14-16, it is noted that page 12 and 13 of the specification define this term as a material for transmitting the rotational motion of the D subunit of the V_1-ATPase to another component or be a probe or propeller for observing the rotation of the V_1-ATPase. Applicants further note that the paragraph describing the joint material has been amended for clarity.

For the above-noted reasons, these rejections are untenable and should be withdrawn.

V. INDEFINITENESS REJECTIONS

On pages 8 and 9, claim 17-22 were rejected as indefinite for insufficient antecedent basis.

Applicants respectfully traverse this rejection. In particular, it is noted that SEQ ID NO: 5 is now recited in claim 11 and therefore antecedent basis exist in claim 17-19. Further, SEQ ID NOs are presented in claim 11 for the A and B subunits. Thus, antecedent basis exists for the objected limitation in claims 20-22.

For the above-noted reasons, this rejection is untenable, as applied to the amended claims, and should be withdrawn.

VI. ANTICIPATION REJECTION

On pages 9 and 10, claims 11-22 were rejected under 35 U.S.C. § 102(a) as anticipated by Imamura et al.

Enclosed are a certified copy JP 2002-337212, from which the present application claims priority to November 20, 2002. Thus, Imamura et al. cannot be applied as prior art and this rejection is overcome.

VII. OBVIOUSNESS REJECTION

On pages 11-13, claim 1 was rejected under 35 U.S.C. § 103(a) as obvious over Yokoyama in view of Xiong et al. Applicants respectfully traverse this rejection as applied to the amended claims.

Applicants note that the A subunit of the claimed invention has two substitutions, an Alanine for the 232nd Serine and a Serine for the 235th Threonine. Xiong et al. does not teach or suggest the substitution of the Serine for the 235th Threonine. Further, as noted on page 12 of the specification, this two substitution subunit continues ATP activity even for one hour after the addition of ATP as a substrate. Normally, ADP restriction appears within five minutes after ATP has been added as a substrate and in about ten minutes V_1-ATPase stops ATP hydrolysis. Such effect is not taught or suggested by the cited references.

Thus, this rejection, as applied to the amended claims, is untenable and should be withdrawn.

CONCLUSION

In view of the foregoing amendments and remarks, it is respectfully submitted that the present application is in condition for allowance and early notice to that effect is hereby requested.

If the Examiner has any comments or proposals for expediting prosecution, please contact the undersigned attorney at the telephone number below.

Respectfully submitted,

Hiromi IMAMURA et al.

By: _____

William R. Schmidt, II
Registration No. 58,327
Attorney for Applicants

WRS/lc
Washington, D.C. 20006-1021
Telephone (202) 721-8200
Facsimile (202) 721-8250
December 23, 2008

ATTACHMENTS

A. Certified Copy of JP 2002-337212

B. Verified English Translation of JP 2002-337212

C. Liu, H. et al., "Control of a biomolecular motor-powered nanodevice with an engineered chemical switch", Nature – Materials, 2002, 1:173-177.

D. Soong, R. K. et al., "Powering an Inorganic Nanodevice with a Biomolecular Motor", Science, 2000, 290:1555-1558.

Control of a biomolecular motor-powered nanodevice with an engineered chemical switch

HAIQING LIU[1], JACOB J. SCHMIDT[1], GEORGE D. BACHAND[2], SHAHIR S. RIZK[3], LOREN L. LOOGER[3], HOMME W. HELLINGA[3] AND CARLO D. MONTEMAGNO*[1]

[1]Department of Bioengineering, University of California, Los Angeles, California 90095, USA

[2]Present address: Biomolecular Materials and Interfaces, Sandia National Laboratories, PO Box 5800, MS 1413, Albuquerque, New Mexico 87185-1413, USA

[3]Department of Biochemistry, Box 3711, Duke University Medical Center, Durham, North Carolina 27710, USA

*e-mail: cdm@seas.ucla.edu

Published online 27 October 2002; doi:10.1038/nmat761

The biophysical and biochemical properties of motor proteins have been well-studied, but these motors also show promise as mechanical components in hybrid nano-engineered systems[1–4]. The cytoplasmic F_1 fragment of the adenosine triphosphate synthase (F_1-ATPase) can function as an ATP-fuelled rotary motor[4–7] and has been integrated into self-assembled nanomechanical systems as a mechanical actuator[4,8]. Here we present the rational design, construction and analysis of a mutant F_1-ATPase motor containing a metal-binding site that functions as a zinc-dependent, reversible on/off switch. Repeated cycles of zinc addition and removal by chelation result in inhibition and restoration, respectively, of both ATP hydrolysis and motor rotation of the mutant, but not of the wild-type F_1 fragment. These results demonstrate the ability to engineer chemical regulation into a biomolecular motor and represent a critical step towards controlling integrated nanomechanical devices at the single-molecule level.

The X-ray crystallographic structures of the F_1 fragment of the bovine mitochondrial ATPase (BF_1) have revealed the nature of the conformational changes involved in ATP hydrolysis in atomic detail[9]. The β-subunits assume two conformations in the crystal structures, an open and a closed state that inter-convert through a hinge-bending motion. In the closed state the β-subunit binds ATP (β_T) or ADP (β_D); in the open state the active site is empty (β_E). Although β_T and β_D adopt the same overall state, there are structural differences between them in several surface loops related to the critical role of these states in the rotary motion of this complex. From these structures, it has also been determined that the three α-subunits assume identical conformations regardless of catalytic state. The six interfaces (three inter-dimer and three intra-dimer) are therefore all different. Because rotation of the γ-subunit relies on sequential interchange between different conformational and substrate ligation states, we hypothesized that reversible inhibition of the catalytic and rotation cycle might be achieved by inserting a secondary metal-binding site capable of interfering with the sequential cycle. Such a site is therefore predicted to function as a classic allosteric inhibitor of enzyme activity[10] and should provide a chemical switch for the control of motor activity in a nanomechanical device.

We chose to construct an allosteric control element based on a zinc-binding site, as these domains are relatively compact, consisting of three or four amino acids that chelate the metal[11]. Moreover, computational design methods have been developed that reliably predict and construct *de novo* metal centres into proteins of known structure[12–14]. Reversible inhibition of the enzymatic activity may be readily achieved by the addition of extrinsic metal chelators (such as 1,10 phenanthroline) that sequester zinc, but not the Mg^{2+} required for ATP binding and hydrolysis. To design locations for allosterically active zinc-binding sites in BF_1, we first identified regions in the interfaces that undergo local conformational changes, but are not part of the active site[15].

In these 'proto-allosteric' sites, a structure-based computational protein design algorithm, Dezymer[12], was used to identify combinations of backbone positions where a tetrahedral zinc site consisting of three histidines and a water molecule could be positioned. The algorithm predicted a set of sites which were then rank-ordered and examined by inspection. We chose a site in the inter-dimer interface between β_D and α_E (Fig. 1). This designed site replaces glutamine α405, glycine β392 and aspartate β400 in BF_1 with histidine residues. The initial design phase yielded a site with approximate tetrahedral geometry. This site was then optimized using a combination of molecular dynamics and conjugate gradient energy minimizations to satisfy the metal coordination geometry necessary to bind ions and result in the immobilization of this region.

The allosteric site was constructed by mutagenesis in the F_1 fragment of the thermophile *Bacillus* PS3 (TF_1) that was previously used to construct biomolecular motor-powered nanodevices[4]. The TF_1 crystalline structure was not used in the initial design studies because it lacks the γ-subunit and all the αβ dimers are in the open conformation, which precludes identification of protoallosteric sites. Modelling of the designed site in the TF_1 structure[16] (residues glutamine α397, glycine β387 and asparate β395) was, however, consistent with the predictions based on BF_1 (not shown). Both the wild-type TF_1 gene (DEMH) and

Attachment C

Figure 1 Molecular model of the computationally designed Zn^{2+} binding site in the bovine F_1-ATPase. The histidines in the three inter-dimer interface locations are shown in red. The circle indicates the site in the β_D/α_E interface predicted to form a tetrahedral Zn^{2+}-binding site (left insert). The ovals indicate that the sites in the other two inter-dimer interfaces do not form a geometry predicted to favour metal binding (right insert).

the mutant with the engineered zinc site (DEMHZ) encode an N-terminal 10X His-tag on the β-subunit for assembly on to functionalized surfaces and a single cysteine on the γ-subunit for attachment of fluorescent actin filaments, as previously described[4,17].

The ATP hydrolytic activity of the mutant enzyme was assessed by steady-state kinetics using a linked enzyme assay to detect production of phosphate[18]. In the absence of Zn^{2+}, DEMH and DEMHZ showed similar specific activity, indicating that the histidine mutations did not affect catalysis (data not shown). Addition of Zn^{2+} to DEMHZ reduced the activity by 60% at saturating concentrations, but did not affect wild-type TF_1 (Fig. 2a). The Zn^{2+} bound hyperbolically with an apparent dissociation constant of 8.6 ± 1.2 μM. The Scatchard plot was linear (not shown) and consistent with non-cooperative binding of Zn^{2+}. An Eadie–Hofstee transformation of the steady-state kinetics with

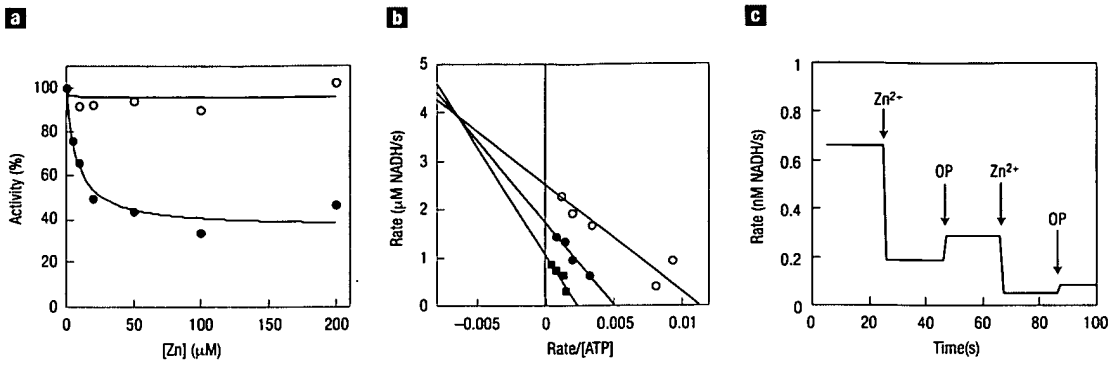

Figure 2 Steady-state kinetics of ATP hydrolysis in the wild-type and mutant TF_1 enzymes. a, The effect of Zn^{2+} addition on the activity of wild-type (DEMH; open circles) and mutant (DEMHZ; filled circles) enzymes. For DEMHZ, Zn^{2+} binding is modelled with a hyperbolic binding isotherm[19], with $^{app}K_d = 8.6$ μM. b, Eadie–Hofstee transformation of the steady-state kinetics of DEMHZ with respect to ATP concentration in the presence of different Zn^{2+} concentrations (open circles, 0 μM; filled circles, 5 μM; squares, 200 μM). c, Two cycles of successive additions of 100 μM Zn^{2+} and 150 μM 1,10-phenanthroline (OP).

respect to [ATP] at various Zn^{2+} concentrations (Fig. 2b) revealed a pattern that is consistent with a linear mixed inhibition mode, in which both K_m(ATP) and V_{max} are affected by Zn^{2+}. This finding is consistent with binding of Zn^{2+} to both the free enzyme and enzyme–substrate complex, as expected[19]. Repeated cycles of Zn^{2+} addition followed by chelation with 1,10-phenanthroline showed that Zn^{2+} reversibly inhibits the enzyme's hydrolytic activity (Fig. 2c). Taken together, these data lead us to conclude that we have successfully designed a Zn^{2+}-dependent allosteric effector site that reversibly modulates TF_1 activity, as predicted.

To demonstrate control of biomolecular motors at the single molecule level, we tethered wild-type and mutated TF_1 motors to Ni–NTA functionalized microspheres bound to the surface of a coverslip (see Methods). Fluorescent actin filaments were then attached to the γ-subunit of motors and observed by epifluorescence microscopy. Filaments rotated clockwise on addition of 2 mM ATP into the flow cell, as previously observed[4,5]. Most of the filaments were stationary or fluctuated around a central position; no filaments rotated anticlockwise. Adding 0.5 M imidazole resulted in the detachment of all moving actin filaments in both the wild-type and mutant experiments, confirming that the observed rotation of the filaments was due to immobilized motor proteins. Further, adding 10 mM sodium azide halted filament rotation of wild-type motors, consistent with previous experiments. Compared with the wild-type motors, the histidine mutations in DEMHZ did not alter the mechanical characteristics of the modified motors in the absence of Zn^{2+} (the mutant motors rotated filaments of the same length at the same rate, indicating that the torque output and efficiency were unchanged). In contrast to the 60% inhibition in hydrolytic activity, all (100%) of the rotating filaments powered by the mutant motors stopped rotating on introduction of a solution containing 2 mM ATP and 800 μM $ZnSO_4$, whereas the wild-type motors remained unaffected. The difference between hydrolytic activity and rotation suggests that complete mechanochemical coupling of this enzyme is not necessary to maintain hydrolytic activity. We then restored rotation of actin filaments by the inhibited mutant motors by flowing 800 μM 1,10-phenanthroline and 2 mM ATP into the chamber (Fig. 3). Using a frictional drag coefficient[20] of $\xi = (4\pi/3)\,\eta L^3 / (\ln(L/2r) - 0.447)$ (with η given by the buffer viscosity (10^{-3} N m s^{-2}), r the radius of the filament (5 nm), and L its length, we obtain an average value for the torque of 34 pN nm. This value is consistent with earlier work[4,6] and indicates that the mutations do not alter the mechanical properties of the motor. The data show that the allosteric Zn^{2+} sites control motor activity and mechanical work done by individual biomolecular motors.

Before motor proteins can be used in integrated nanodevices and nanocomposite materials, mechanisms for controlling motor activity externally must be in place. We have previously constructed hybrid nanomechanical devices powered by F_1-ATPase and have now demonstrated a way of chemically controlling an engineered biomolecular motor. Our method maintains the presence of fuel (ATP), does not affect the mechanical properties of the motors and does not affect the activity of other ATP-dependent enzymes. These experiments represent critical steps in the realization of logical and useful biomolecular motor-powered structures. The technology may be extended through engineering of secondary binding sites to other pre-selected ligands. Aside from use as a mechanical actuator, the introduction of a secondary mechanism to control motor functionality also may allow sensing and feedback control of the motor and associated devices.

METHODS

MOLECULAR MODELLING

Protoallosteric sites were identified using C_α–C_α double-difference distance maps[18], comparing β_ε and β_t structures. Tetrahedral zinc sites coordinated by three histidines and a water molecule were designed using the Dezymer program[12]. The zinc is allowed to coordinate with either the N_δ or N_ε nitrogens of the histidines and is constrained within the plane of the imidazole ring, as described[13]. Mutations were chosen to satisfy both the desired metal binding geometry and the steric compatibility of the protein folding.

MOTOR PROTEINS

The α-, β- and γ-subunits of wild-type TF_1, modified with additional mutations for incorporation into self-assembled nanodevices (DEMH)[4], were co-expressed using the pETBlue (Novagen) plasmid and purified as described previously. Three histidines for creating the zinc binding sites were introduced by site-directed mutagenesis; all mutations were confirmed by DNA sequencing. The recombinant subunits were expressed in *Escherichia coli* Tuner™ (DE3) pLacI (Novagen), and purified in the same way as DEMH.

STEADY-STATE KINETICS

We determined protein concentrations of the $\alpha_3\beta_3\gamma$ complex spectrophotometrically at 280 nm (extinction coefficient 0.45). Steady-state ATPase activity at 25 °C was determined with an ATP-regenerating system[19]. To evaluate the inhibition of the mutant TF_1 motors by zinc, we added 800 μM $ZnSO_4$ to the assay mixture, which contained 50 mM Tris-HCl (pH 7.4), 100 mM KCl, 2.5 mM phosphoenolpyruvate,

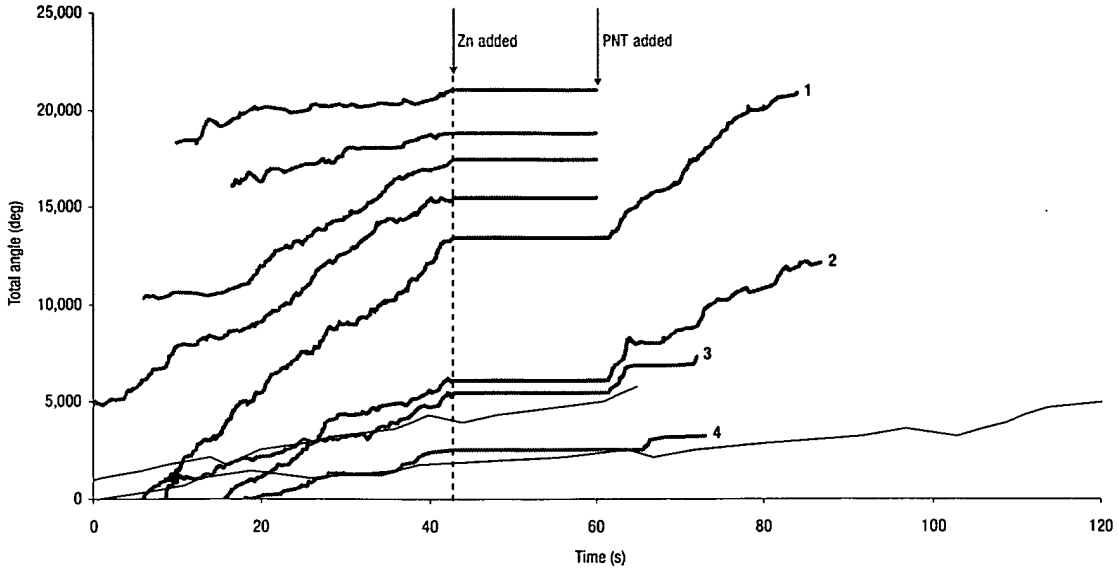

Figure 3 Measurements of single-molecule rotation and control. The movements of rotating fluorescent actin filaments were recorded and digitized. The rotation angle as a function of time is shown for eight filaments attached to the mutant ATPase and two filaments attached to motors without the zinc mutation (black lines). The filaments rotated continuously in the presence of ATP. After the addition of 800 μM $ZnSO_4$ (blue arrow), the filaments attached to the mutant motor stopped, whereas the filaments attached to the wild-type motor continued rotating at the same rate. We added 1,10-phenanthroline (800 μM) to the stopped filaments (red arrow), restarting the motor motion. There was an interval of about 3 s after the addition of both the Zn^{2+} and the phenanthroline in which the filaments were out of focus because the stage position had been disturbed, preventing a more precise determination of the times of stopping and restarting motion. Some filaments were dislodged from the surface during the fluid replacement and so rotation data following the PNT addition are not available (green lines). The data for all filaments have been shifted in time to synchronize the Zn^{2+} addition times. The Zn^{2+} seems to have no lasting effects on the motors. The rotational rates before Zn^{2+} addition and after Zn^{2+} removal are similar, as linear fits of each of the pink traces show: (1) before Zn^{2+} 0.96 rotations s^{-1}, after Zn^{2+} 0.97 rotations s^{-1}; (2) 0.61, 0.61; (3) 0.36, 0.32; (4) 0.27, 0.19. The differences between the numbers in each case are within the variations of rotational rate before Zn addition. The lengths of filaments 1–4 are 1.75 μm, 2.0 μm, 2.25 μm and 2.25 μm, respectively.

25 μg ml^{-1} pyruvate kinase, 25 μg ml^{-1} lactate dehydrogenase (Roche), 0.2 mM NADH (Sigma), 2 mM Na_2ATP and 4 mM $MgCl_2$. Inhibition and reactivation of the TF_1 motors was demonstrated by the addition of 800 μM of zinc, and 800 μM of 1,10-phenanthroline (a zinc chelator).

SINGLE-MOLECULE ROTATION ASSAY

We constructed a flow chamber consisting of a coverslip (22 × 40 mm, #0) attached to a microscope slide using double-sided tape. Polystyrene beads (0.22 μm diameter) coated with Ni-NTA (ref. 6) in buffer A (50 mM KCl, 5 mM $MgCl_2$, 10 mM MOPS-KOH, pH 7) (1:10) were infused into the flow cell and incubated for 15 min, resulting in a density of several beads in an area 5 × 5 $μm^2$. Non-adherent beads were removed by rinsing three times with two volumes of buffer B (buffer A + 10 mg ml^{-1} BSA). The His-tagged biotinylated ATPase (at a concentration of 28 nM) in buffer B was then incubated for 5 min and rinsed three times with two volumes of buffer B. Streptavidin (180 nM) in buffer B was incubated in the chamber for 12–15 min and rinsed three times with two volumes of buffer B. Actin filaments (fluorescently labelled with Phalloidin-TRITC, polymerized and biotinylated)[5] were diluted to 50 nM in buffer B and incubated in the flow chamber for 12–15 min. The chamber was washed twice with two volumes of buffer B and a third time with two volumes of buffer C. Buffer C consists of buffer B with an oxygen scavenger (0.5% 2-mercaptoethanol, 30 units ml^{-1} catalase, 6 mg ml^{-1} glucose, and 0.2 mg ml^{-1} glucose oxidase) and an ATP-regenerating system (2 mM Na_2ATP, 0.2 mg ml^{-1} creatine kinase and 2.5 mM creatine phosphate). We observed the actin filaments with a Nikon E800 upright optical microscope in epifluorescence mode. We added $ZnSO_4$ (800 μM) in buffer C to determine any effect on the mutant and wild-type protein. We added 1,10-phenanthroline (800 μM) in buffer C to determine the reversibility of the zinc switch.

Received 12 September 2002; accepted 4 October 2002; published 27 October 2002.

References

1. Hess, H., Clemmens, J., Qin, D., Howard, J. & Vogel, V. Light-controlled molecular shuttles made from motor proteins carrying cargo on engineered surfaces. *Nanoletters* 1, 235–239 (2001).
2. Bohm, K. J., Stracke, R., Muhlig, P. & Unger, E. Motor protein-driven unidirectional transport of micrometer-sized cargoes across isopolar microtubule arrays. *Nanotechnology* 12, 238–244 (2001).
3. Hiratsuka, Y., Tada, T., Oiwa, K., Kanayama, T. & Uyeda, T. Controlling the direction of kinesin-driven microtubule movements along microlithographic tracks. *Biophys. J.* 81, 1555–1561 (2001).
4. Soong, R. K. *et al.* Powering an inorganic nanodevice with a biomolecular motor. *Science* 290, 1555–1558 (2000).
5. Noji, H., Yasuda, R., Yoshida, M. & Kinosita, K. Direct observation of the rotation of F_1-ATPase. *Nature* 386, 299–302 (1997).
6. Yasuda, R., Noji, H., Kinosita, K. & Yoshida, M. F_1-ATPase is a highly efficient molecular motor that rotates with discrete 120 degrees steps. *Cell* 93, 1117–1124 (1998).
7. Yasuda, R., Noji, H., Yoshida, M., Kinosita, K. & Itoh, H. Resolution of distinct rotational substeps by submillisecond kinetic analysis of F_1-ATPase. *Nature* 410, 898–904 (2001).
8. Soong, R. K., Neves, H. P., Bachand, G. D., Schmidt, J. & Montemagno, C. D. Engineering hybrid nanoscale devices powered by biomolecular motors. *Biomed. Microdevices* 3, 71–73 (2001).
9. Abrahams, P., Leslie, A. G. W., Lutter, R. & Walker, J. E. Structure at 2.8 Å resolution of F_1-ATPase from bovine heart mitochondria. *Nature* 370, 621–628 (1994).
10. Perutz, M. F. Mechanism of cooperativity and allosteric regulation in proteins. *Q. Rev. Biophys.* 22, 139–237 (1989).
11. Glusker, J. P. Structural aspects of metal liganding to functional groups in proteins. *Adv. Prot. Chem.* 42, 1–76 (1991).
12. Hellinga, H. W. & Richards, F. M. Construction of new ligand-binding sites in proteins of known structure. 1. Computer-aided modeling of sites with predefined geometry. *J. Mol. Biol.* 222, 763–785 (1991).
13. Marvin, J. S. & Hellinga, H. W. Conversion of a maltose receptor into a zinc biosensor by computational design. *Proc. Natl Acad. Sci. USA* 98, 4955–4960 (2001).
14. Benson, D., Haddy, A. E. & Hellinga, H. W. Converting a maltose receptor into a nascent binuclear copper oxygenase by computational design. *Biochemistry* 41, 3262–3269 (2002).
15. Marvin, J. *et al.* The rational design of allosteric interactions in a monomeric protein and its applications to the construction of biosensors. *Proc. Natl Acad. Sci. USA* 98, 4366–4371 (1997).
16. Shirakihara, Y. *et al.* The crystal structure of the nucleotide-free subcomplex of F_1-ATPase from the

thermophilic Bacillus PS3 is a symmetric trimer. *Structure* 5, 825–836 (1997).
17. Bachand, G. D. & Montemagno, C. D. Constructing organic/inorganic NEMS devices powered by biomolecular motors. *Biomed. Microdevices* 2, 179–184 (2000).
18. Pullman, M. E., Penefsky, H. S., Datta, A. & Racker, E. Partial resolution of the enzyme catalyzing oxidative phosphorylation. I. Purification and properties of soluble, dinitrophenol-stimulated adenosine triphosphatase. *J. Biol. Chem.* 235, 3322–3329 (1960).
19. Segel, I. H. *Enzyme Kinetics* (Wiley, New York, 1975).
20. Hunt, A. J., Gittes, F. & Howard, J. The force exerted by a single kinesin molecule against a viscous load. *Biophys. J.* 67, 766–781 (1994).

Acknowledgements

We thank C. Xu for help in the protein modelling of the TF_1 structure. This research was supported in part by grants from NASA (NAG5-8775), DARPA (N00014-99-1-0436) and NSF (ECS-0084732). Sandia is a multiprogram laboratory operated by Sandia Corporation, a Lockheed Martin Company, for the US Department of Energy under contract DE-AC04-94AL85000.
Correspondence and requests for materials should be addressed to C.D.M.

Competing financial interests

The authors declare that they have no competing financial interests.

Science
AAAS

Powering an Inorganic Nanodevice with a Biomolecular Motor

Ricky K. Soong, *et al.*

Science **290**, 1555 (2000);
DOI: 10.1126/science.290.5496.1555

Science (print ISSN 0036-8075; online ISSN 1095-9203) is published weekly, except the last week in December, by the American Association for the Advancement of Science, 1200 New York Avenue NW, Washington, DC 20005.

Attachment D

when the bias increases and no state is available for tunneling. This mechanism for negative differential conductance is similar to that in a double-barrier resonance tunnel diode (*26*).

The CB data (Fig. 4A) does show slight deviation from the characteristics of a perfect single-dot with incomplete Coulomb gap closure. Therefore, we cannot entirely rule out the possibility of dots in series on the nanotube (*27, 28*). A likely mechanism for NDC in this case is resonance tunneling through multiple discrete energy levels in adjacent dots. Two energy levels of double-dots involved in resonance tunneling and NDC have been observed in two-dimensional electron gas systems (*29*).

The high-temperature electrical characteristics of the sample shown here represent the results obtained with three modulation-doped SWNTs (diameters of ~2 nm). The modulated doping scheme reliably leads to intramolecular p^+n^+ junctions exhibiting negative differential conductance. At low temperatures, CB phenomena are consistently observed with the samples, but with the manifestation of unintentional doping modulation effects (not noticeable at high temperatures). This points to a need for much better control of the chemical homogeneity along the nanotube length. Most important, it also suggests that controlled doping modulations over a length scale of <100 nm along a nanotube should lead to well-defined quantum systems including coupled quantum dots. Modulated chemical doping of nanotubes holds promise as a new route to intramolecular devices.

References and Notes

1. W. Shockley, *IEEE Trans. Electron. Devices* **ED-23**, 597 (1976).
2. L. Esaki, *IEEE Trans. Electron. Devices* **ED-23**, 644 (1976).
3. C. Dekker, *Phys. Today* **52**, 22 (May 1999).
4. F. Leonard, J. Tersoff, *Phys. Rev. Lett.* **83**, 5174 (1999).
5. K. Esfarjani, A. A. Farajian, Y. Hashi, Y. Kawazoe, *Appl. Phys. Lett.* **74**, 79 (1999).
6. R. D. Antonov, A. T. Johnson, *Phys. Rev. Lett.* **83**, 3274 (1999).
7. L. Chico, V. H. Crespi, L. X. Benedict, S. G. Louie, M. L. Cohen, *Phys. Rev. Lett.* **76**, 971 (1996).
8. J. Hu, M. Ouyang, P. Yang, C. M. Lieber, *Nature* **399**, 48 (1999).
9. Z. Yao, H. W. C. Postma, L. Balents, C. Dekker, *Nature* **402**, 273 (1999).
10. J. Kong, H. Soh, A. Cassell, C. F. Quate, H. Dai, *Nature* **395**, 878 (1998).
11. S. Tans, A. Verschueren, C. Dekker, *Nature* **393**, 49 (1998).
12. R. Martel, T. Schmidt, H. R. Shea, T. Hertel, P. Avouris, *Appl. Phys. Lett.* **73**, 2447 (1998).
13. C. Zhou, J. Kong, H. Dai, *Appl. Phys. Lett.* **76**, 1597 (1999).
14. P. G. Collins, K. Bradley, M. Ishigami, A. Zettl, *Science* **287**, 1801 (2000).
15. J. Kong *et al.*, *Science* **287**, 622 (2000).
16. J. Kong, C. Zhou, E. Yenilmez, H. Dai, *Appl. Phys. Lett.*, in press.
17. R. S. Lee *et al.*, *Phys. Rev. B* **61**, 4526 (2000).
18. M. Bockrath *et al.*, *Phys. Rev. B* **61**, R10606 (2000).
19. B. G. Streetman, *Solid State Electronic Devices* (Prentice-Hall, Englewood Cliffs, NJ, 1995).
20. H. Grabert, M. H. Devoret, Eds., *Single Charge Tunneling* (Plenum, New York, 1992).
21. S. J. Tans *et al.*, *Nature* **386**, 474 (1997).
22. M. Bockrath *et al.*, *Science* **275**, 1922 (1997).
23. J. Nygard, D. H. Cobden, M. Bockrath, P. L. McEuen, P. E. Lindelof, *Appl. Phys. A* **69**, 297 (1999).
24. A. Bachtold *et al.*, *Phys. Rev. Lett.* **84**, 6082 (2000).
25. S. Tans, C. Dekker, *Nature* **404**, 834 (2000).
26. L. L. Chang, L. Esaki, R. Tsu, *Appl. Phys. Lett.* **24**, 593 (1974).
27. A. Bezryadin, A. Verschueren, S. Tans, C. Dekker, *Phys. Rev. Lett.* **80**, 4036 (1998).
28. P. L. McEuen, M. Bockrath, D. H. Cobden, Y.-G. Yoon, S. G. Louie, *Phys. Rev. Lett.* **83**, 5098 (1999).
29. N. C. vander Vaart, S. F. Godijn, Y. V. Nazarov, C. J. P. M. Harmans, J. E. Mooji, *Phys. Rev. Lett.* **74**, 4702 (1995).

30. Supported by the National Science Foundation, Defense Advanced Research Projects Agency/Office of Naval Research, Semiconductor Research Corporation/Motorola, a David and Lucile Packard Fellowship, a Terman Fellowship, the Laboratory for Advanced Materials at Stanford, National Nanofabrication Users Network at Stanford, the Camile Henry-Dreyfus Foundation, and the American Chemical Society.

15 August 2000; accepted 12 October 2000

Powering an Inorganic Nanodevice with a Biomolecular Motor

Ricky K. Soong,[1,2] George D. Bachand,[1,2] Hercules P. Neves,[1,2] Anatoli G. Olkhovets,[1,3] Harold G. Craighead,[1,3] Carlo D. Montemagno[1,2]*

Biomolecular motors such as F_1–adenosine triphosphate synthase (F_1-ATPase) and myosin are similar in size, and they generate forces compatible with currently producible nanoengineered structures. We have engineered individual biomolecular motors and nanoscale inorganic systems, and we describe their integration in a hybrid nanomechanical device powered by a biomolecular motor. The device consisted of three components: an engineered substrate, an F_1-ATPase biomolecular motor, and fabricated nanopropellers. Rotation of the nanopropeller was initiated with 2 mM adenosine triphosphate and inhibited by sodium azide.

Emergent fabrication techniques permit the construction of structures with features smaller than 7 nm (*1–4*). However, the construction of functional nanoelectromechanical systems (NEMS) is hindered by the inability to provide locomotive forces to power NEMS devices. The use of biomolecular motors such as enzymes offers an interesting alternative to silicon-based systems (*5, 6*). A number of enzymes such as kinesin (*7, 8*), RNA polymerase (*9*), myosin (*10*), and adenosine triphosphate (ATP) synthase (*5, 6, 11, 12*) function as nanoscale linear or rotary biological motors. The integration of biomolecular motors with nanoscale engineered systems enables the development of hybrid organic-inorganic devices capable of using ATP as an energy source. This approach may enable the creation of a new class of sensors, mechanical force transducers, and actuators.

The F_1-ATPase enzyme, which hydrolyzes ATP in living systems, is an excellent candidate for integration with NEMS for construction of rotary biomolecular motor–powered nanodevices (*5, 6*). The F_1-ATPase molecule, ~8 nm in diameter and 14 nm in length, is capable of producing ~80 to 100 pN·nm of rotary torque (*11, 12*). These characteristics of F_1-ATPase are compatible with the sizes and force constants of currently producible nanomechanical structures (*5, 6*). In addition, genetic modification of the F_1-ATPase sequence and structure has been used to precisely position individual F_1-ATPase molecules on engineered nanofabricated substrates (*13*). Previous studies have shown that actin filaments (5 nm in diameter and 1 to 4 μm in length) can be attached to the motor using biochemical techniques, and the resulting rotary motion can be visualized (*11, 12*). The integration of F_1-ATPase motors and nanofabricated mechanical systems, however, presents considerable engineering challenges with regard to the organic and inorganic interface (e.g., attachment chemistries, adhesion forces, and materials compatibility).

Our biomolecular motor–powered NEMS device consisted of three primary elements: (i) engineered, nanofabricated substrates of nickel (Ni) posts; (ii) recombinant F_1-ATPase biomolecular motors specifically engineered to selectively interface with nanofabricated structures; and (iii) engineered nanopropellers (Fig. 1). These elements were integrated into a functional unit using sequential attachment chemistries. Recombinant F_1-ATPase biomolecular motors were biotinylated immediately after purification and were then attached to the Ni posts using 10× histidine

[1]Nanobiotechnology Center, [2]Department of Agricultural and Biological Engineering, [3]School of Applied and Engineering Physics, Cornell University, Ithaca, NY 14853, USA.

*To whom correspondence should be addressed. E-mail: cdm11@cornell.edu

tags engineered into the β-subunit coding sequence (*5, 6*). Streptavidin was then bound to the biotin residue on the γ subunit tip. Ni nanopropellers coated with biotinylated histidine-rich peptides were attached to the bound F_1-ATPase motors through a biotin-streptavidin linkage.

A thermostable F_1-ATPase from *Bacillus* PS3 was cloned, modified, and purified as described (*5, 6, 14*). The recombinant F_1-ATPase was labeled with biotin maleimide using an engineered unique cysteine residue on the γ subunit. The activity of the enzyme was determined using an ATP regeneration assay (*11, 15*).

Engineered, nanofabricated substrates were constructed as the base for the device and for attachment of biomolecular motors. Ni posts (50 to 120 nm in diameter and 200 nm high) were fabricated to prevent problems associated with increased drag on propellers due to the close proximity to the base surface. Precleaned round glass cover slips (25 mm) were coated with silicon dioxide (SiO_2) using plasma-enhanced chemical vapor deposition and were then coated with 4% polymethyl methacrylate (PMMA). A thin gold conductive layer was thermally evaporated onto the resist-coated slide for electron-beam (e-beam) lithography. The exposure pattern written onto the cover slip consisted of dots with a 2.5- or 5-μm horizontal and vertical pitch and a series of border marks to identify the post region (*16*). The average post measured 50 to 120 nm in diameter, depending on the e-beam exposure dose. Slides were etched with potassium iodine for removal of gold and were then immersed in methyl isobutyl ketone: isopropanol (MIBK:IPA) to develop the features. Electron gun evaporation was used to form the Ni caps on the posts. The surrounding PMMA and residual Ni were removed using acetone and methylene chloride. The posts were formed by etching the SiO_2 layer to the appropriate height with the use of a plasma-induced reactive ion etch process.

The propeller dimensions were optimized for both optical detection and minimal friction during rotation. The propellers (150 nm in diameter and 750 to 1400 nm long) were fabricated on PMMA-coated silicon wafers using e-beam lithography, and features were then developed with MIBK:IPA (*17*). Electron gun evaporation was used to deposit Ni for formation of the propellers; residual PMMA and Ni were removed with methylene chloride and acetone. After isotropic etching with 60% KOH to remove the propellers, the etchant was removed by dialysis and the propellers were collected by centrifugation at 500,000*g* for 15 min and resuspended in 1× phosphate-buffered saline (PBS). The propellers were then coated with a biotinylated His-rich peptide (NH_2-CGGSGGSHHHHHH-COOH, where C = Cys, G = Gly, H = His, and S = Ser) to facilitate attachment to the γ subunit of F_1-ATPase, then dialyzed to remove extraneous peptide and biotin (*18*).

The functional device was constructed by ordered, sequential addition of the individual components. A 100-μl aliquot of biotinylated F_1-ATPase biomolecular motors (1 mg/ml in 10 mM phosphate buffer, pH 7.0) was placed directly on the engineered Ni substrates. The F_1-ATPase molecules were allowed to diffuse and bind to the Ni for 15 to 30 min. Substrates were washed three times with Buffer A [10 mM MOPS-KOH (pH 7.0), 50 mM KCl, 5 mM $MgCl_2$, and bovine serum albumin (10 mg/ml)]. A 100-μl aliquot of streptavidin (50 μg/ml diluted in Buffer A) was placed on the substrate and incubated for 15 min, followed by three washes with Buffer A. Finally, a 100-μl aliquot of the peptide-labeled nanopropellers was placed on the substrate and incubated for 15 to 30 min. The substrate was washed three times with Buffer A and mounted in a custom-fabricated flow cell.

Observations of propeller rotation were made using 100× oil immersion or 60× water immersion and were captured using a charge-coupled device (CCD) video camera. Buffer A was used to fill the flow cell containing the device until the patterned array (i.e., alignment marks) was located, at which time the buffer was replaced with Buffer A plus 2 mM Na_2ATP. To demonstrate the rotation dependency of the propeller, we added 10 mM sodium azide (NaN_3) to the flow cell to inhibit the activity of the F_1-ATPase motor. Rotation of propellers in the absence of ATP (i.e., Buffer A alone) also was examined to demonstrate the functional dependency of the device on the F_1-ATPase biomolecular motor.

Of about 400 total propellers, five rotated continuously in an anticlockwise direction (Fig. 2). Rotating propellers were generally attached at a point 1/4 to 1/3 of the total propeller length from the end of the propeller, but did not show any preferential point of attachment. The majority (~80%) of the nonrotating propellers did not display any Brownian fluctuation; this suggests that the propellers either were attached to more than one F_1-ATPase motor or were bound to the motor as well as the substrate. However, it is highly unlikely that the propellers (750 nm long) were attached to multiple motors, because of the spacing (≥2.5 μm) of the Ni posts.

The rotational velocity of the device varied considerably from 0.74 to 8.3 revolutions per second (rps), with a mean velocity of 4.8 ± 0.8 rps (Fig. 3). Variation in angular velocity was caused by different lengths of the nanopropellers used in various experiments. Detailed analysis of two propellers of differing lengths revealed two distinct rotational velocities, depending on the point of attachment and length of the propeller (Fig. 3). The mean rotation velocity of rods that were 750 and 1400 nm long was 8.0 ± 0.4 and 1.1 ± 0.1 rps, respectively. Momentary pauses were occasionally observed during rotation. Backward steps and teetering between catalytic sites have been reported previously (*9, 10*), but were not observed during these experiments. The absence of these backward steps may be due to the maintenance

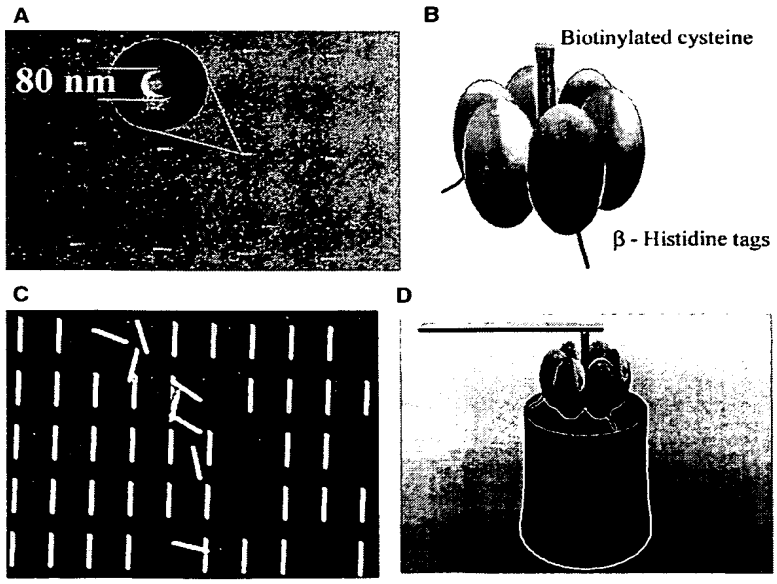

Fig. 1. Schematic diagram of the F_1-ATPase biomolecular motor–powered nanomechanical device. The device consisted of (**A**) a Ni post (height 200 nm, diameter 80 nm), (**B**) the F_1-ATPase biomolecular motor, and (**C**) a nanopropeller (length 750 to 1400 nm, diameter 150 nm). The device (**D**) was assembled using sequential additions of individual components and differential attachment chemistries.

of a high ATP concentration in the chamber; during the course of all experiments, the ATP solution was replaced every 10 min to provide a continuous fuel supply for the motor.

About 2 hours after the initial infusion of ATP into the chamber, the first rotating propeller was located and data collection began. Data were recorded for 30 min, until the propeller broke away from the motor. This result suggests that the device was functional for 2.5 hours during the first experiment, assuming that rotation began immediately upon initial infusion of ATP. Observations of other propeller–molecular motor assemblies confirmed the long life of this construct and are longer-lived than those previously reported with actin filaments (*11*, *12*).

The addition of 2 mM ATP and 10 mM NaN_3 caused the device to cease rotation, hence the rotation of the propellers was due to F_1-ATPase motors. The difference between the rotation rates with and without NaN_3 was significant ($P < 0.01$, Mann-Whitney rank sum test). Previously rotating propellers fluctuated because of Brownian forces, but they did not rotate consistently ($<0.3 \pm 0.01$ rps) as they had before the addition of NaN_3. Rotation was also not observed in the absence of ATP.

Because the exact dimensions of the propeller, post, and motor are known, the work done by the F_1-ATPase motor was accurately determined. The drag force per unit length for a propeller moving near a surface was calculated as

$$dF/dL = \frac{4\pi\mu U}{\cosh^{-1}(h/r)} \quad (1)$$

(*19*), where h is the height of the cylinder axis relative to the surface (200 nm), U is the linear velocity, r is half the width of the propeller (75 nm), and μ is the viscosity of the medium (10^{-3} N·m s^{-2}). For small h, most energy dissipation happens in the propeller-substrate gap (*20*), so we can approximate the total drag by the sum of the drag forces on small segments of the propeller. The total drag torque τ is calculated by the integration along the length of the propeller

$$\tau = \frac{4}{3}\frac{\pi\mu\omega(L_1^3 + L_2^3)}{\cosh^{-1}(h/r)} \quad (2)$$

where ω is the rotational velocity and L_1 and L_2 are the lengths of the propellers extending from the rotational axis.

The calculated total torque on the motor was ~20 pN·nm for the 750-nm propellers (mean rotational velocity of 8.00 rps, attached ~200 nm from the end) and 19 pN·nm for the 1400-nm propellers (mean rotational velocity of 1.1 rps, attached ~350 nm from the end). The energy used ($E = 2\pi\tau$) to complete one revolution of the propellers was 119 to 125 pN·nm. About 240 pN·nm of energy is released by hydrolysis of three ATP molecules, assuming −12 kcal/mol ATP under physiological conditions (*21*). Thus, the measured efficiency of the motor is ~50%. However, the free energy of ATP hydrolysis depends on the concentration of Mg^{2+} and Ca^{2+} in solution, and has been reported as −7.3 kcal/mol (*21*) or ~150 pN·nm, giving a measured efficiency of ~80%. These energy and efficiency values are in contrast to previous reports of 100% efficiency by F_1-ATPase from *Bacillus* PS3, *Escherichia coli*, and spinach chloroplasts (*11*, *22*–*24*). The values of 100% efficiency for the various F_1-ATPase types also were calculated on the basis of −12 kcal/mol ATP. The efficiency values reported here are based on more accurate estimates of the propeller length compared to the actin filaments, as well as an empirical accounting of the vertical position of the propeller with respect to the surface. Out-of-plane wobble and drag associated with the close proximity of the propeller to the top of the post may account for additional torque placed on the motor, but these phenomena are relatively insignificant with respect to the overall torque.

Our experiments demonstrate the ability to integrate biomolecular motors with nanoengineered systems to produce functional nanomechanical devices. Manipulation of individual components and attachment chemistries should help to refine the construction of these devices and improve the complexity of devices, as well as increase the efficiency and success of the assembly process.

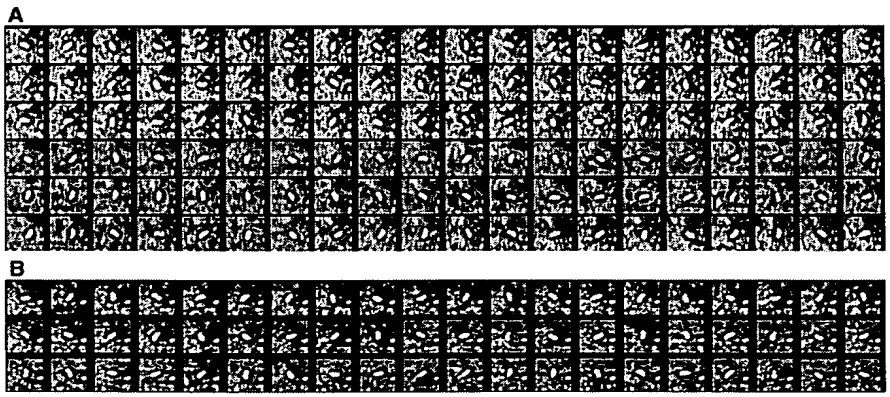

Fig. 2. Image sequence (viewed left to right) of nanopropellers being rotated anticlockwise at 8.3 rps (**A**) and 7.7 rps (**B**) by the F_1-ATPase biomolecular motor. Observations were made using 100× oil immersion or 60× water immersion and were captured with a CCD video camera (frame rate 30 Hz). The rotational velocity ranged from ~0.8 to 8.3 rps, depending on propeller length. Data were recorded for up to 30 min; however, propellers rotated for almost 2.5 hours while ATP was maintained in the flow cell. These sequences can be viewed as movies at the Nanoscale Biological Engineering and Transport Group Web site (http://falcon.aben.cornell.edu/News2.htm).

Fig. 3. Time course of F_1-ATPase γ subunit rotation. Each line represents data from a rotating nanopropeller. Solid lines, propellers 750 nm long; dashed lines, propellers 1400 nm long; dotted lines, propellers 1400 nm long in the presence of NaN_3.

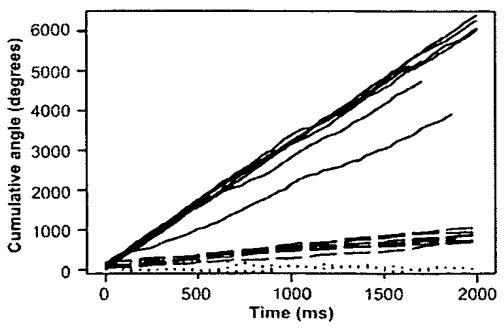

References and Notes

1. R. B. Marcus, T. S. Ravi, T. Gmitter, *Appl. Phys. Lett.* **56**, 236 (1990).
2. J. Sone *et al.*, *Nanotechnology* **10**, 135 (1999).
3. D. W. Carr, L. Sekaric, H. G. Craighead, *J. Vac. Sci. Technol. B* **16**, 3821 (1998).
4. D. W. Carr, S. Evoy, L. Sekaric, J. M. Parpia, H. G. Craighead, *Appl. Phys. Lett.* **75**, 920 (1999).
5. C. D. Montemagno, G. D. Bachand, *Nanotechnology* **10**, 225 (1999).
6. G. D. Bachand, C. D. Montemagno, *Biomed. Microdevices* **2**, 179 (2000).
7. S. M. Block, *Cell* **93**, 5 (1998).
8. M. J. Schnitzer, S. M. Block, *Nature* **388**, 386 (1997).
9. M. Wang *et al.*, *Science* **282**, 902 (1998).
10. K. Kitamura, M. Tokunaga, A. H. Iwane, T. Yanagida, *Nature* **397**, 129 (1999).
11. R. Yasuda, H. Noji, K. Kinosita Jr., M. Yoshida, *Cell* **93**, 1117 (1998).
12. H. Noji, R. Yasuda, M. Yoshida, K. Kinosita Jr., *Nature* **386**, 299 (1997).
13. R. K. Soong, S. J. Stelick, G. D. Bachand, C. D. Montemagno, *Technical Proceedings of the Second International Conference on Modeling and Simulation of Microsystems*, San Juan, Puerto Rico, 19–21 April 1999 (Computational Publications, Boston, 1999), pp. 95–98.

14. Site-directed mutagenesis was used to (i) change the α initiation codon from ATG to CTG, (ii) change the αCys[193] to Ser, (iii) change the γSer[107] to Cys, (iv) change the γ initiation codon from GTG to ATG, and (v) change the γ termination codon from TAG to TAA in the cloned F_1-ATPase construct (pGEM-DEMH). The construct also contained a 10-histidine tag that was inserted immediately downstream of the β initiation codon. The recombinant protein was expressed in *E. coli* JM103 Δ(*uncB-uncD*) and purified using affinity (i.e., Ni–nitrilotriacetic acid) and size exclusion chromatography.
15. T. Matsui, M. Yoshida, *Biochim. Biophys. Acta* **1231**, 139 (1995).
16. The exposure pattern written on the cover slip consisted of dots with a 5-μm horizontal and vertical pitch and border marks to identify the post region. The dots averaged 50 to 120 nm in diameter, depending on the e-beam exposure dose, which varied from 10 to 30 fC/μm^2. The exposed area measured 300 μm by 300 μm, exclusive of the border marks. The border marks (lines 50 μm wide) were spaced 0.5 μm from the edge of the post region.
17. The patterning was performed on silicon wafers that were spin-coated with 4% PMMA in methoxybenzene at 3000 rpm, resulting in a thickness of ~150 nm. The width of the nanopropellers was 150 nm; their length varied from 750 nm to 1.4 μm, depending on the exposure dose, which varied from 3.75 to 4.5 nC/cm. The optimum dose was determined to be 4.3 nC/cm.
18. The synthetic His-rich peptide was specifically biotinylated to the NH_2-terminal Cys residue through disulfide linkage in the presence of *N,N*-dimethylformamide. A 100-μl aliquot of the biotinylated peptide was incubated with 400 μl of the nanopropellers for 15 min, then dialyzed against 1× PBS to remove any excess peptide and biotin maleimide.
19. D. J. Jeffrey, Y. Onishi, *J. Mech. Appl. Math.* **34**, 129 (1981).
20. A. J. Hunt, F. Gittes, J. Howard, *Biophys. J.* **67**, 766 (1994).
21. L. Stryer, *Biochemistry* (Freeman, New York, ed. 4, 1999), pp. 445–447.
22. H. Omote *et al.*, *Proc. Natl. Acad. Sci. U.S.A.* **96**, 7780 (1999).
23. H. Noji *et al.*, *Biochem. Biophys. Res. Commun.* **260**, 597 (1999).
24. T. Hisabori, A. Kondoh, M. Yoshida, *FEBS Lett.* **463**, 35 (1999).
25. We thank F. Peters for figure preparation and assistance in digitization of the data. Supported by grants from the Keck Fellowship Program, Office of Naval Research, and Defense Advanced Research Projects Agency (N00014-99-1-0436CS), NSF (ECS-9007033 and ECS-7876771), U.S. Department of Energy (DE-FG07-96ER14703), and NASA (NAGS-8775).

1 August 2000; accepted 13 October 2000

Mechanisms of Ordering in Striped Patterns

Christopher Harrison,[1] Douglas H. Adamson,[2] Zhengdong Cheng,[1]* John M. Sebastian,[3] Srinivasan Sethuraman,[4] David A. Huse,[1] Richard A. Register,[3] P. M. Chaikin[1]

We have studied the ordering dynamics of the striped patterns of a single layer of cylindrical block copolymer microdomains in a thin film. By tracking disclinations during annealing with time-lapse atomic force microscopy, we observe a dominant mechanism of disclination annihilation involving three or four disclinations (quadrupoles). Pairwise disclination annihilation events are suppressed as a result of the topological constraints in this system. The kinetic scaling laws with exponents observed here are consistent with topologically allowed annihilation events involving multiple disclinations. The results provide insight into two-dimensional pattern formation and may lead to the successful application of block copolymer lithography.

Striped patterns are produced in a variety of disparate systems, including Rayleigh-Benard convection cells, ferrimagnetic films with dipolar interactions, and biological development such as with a zebra's stripes, or perhaps closer at hand, in one's fingerprints (*1*). A classic realization of a nondriven striped system is the two-dimensional (2D) smectic liquid crystal. This system has been the focus of intense research since being discussed by several seminal articles two decades ago (*2*). Although there has been recent progress in understanding equilibrium phenomena such as the role of orientational and translational order in 2D smectics (*3*, *4*), little is known about the kinetics and mechanisms by which order evolves in a 2D smectic system after being quenched from the disordered state, although this has been explored by simulations (*5–8*). The most pressing application for understanding pattern formation in 2D smectics is block copolymer lithography—a process that uses self-assembled patterns (such as single layers of cylinders or spheres) as a template to fabricate devices at the nanometer-length scale (*9–11*). Therefore, our motivation is both fundamental understanding of pattern coarsening and optimization of microdomain order for copolymer lithography, an application that has been used to produce an unprecedented density of metal dots for information storage (*12*), and most recently, to fabricate InGaAs/GaAs quantum dots for laser emission (*13*). We show that the coarsening process is driven by the interaction of topological defects and that the measured kinetic exponents can be understood in terms of a dominant annihilation mechanism that involves more than two disclinations.

Our model system consists of microphase separated block copolymers in thin films. Block copolymers consist of two or more homogeneous but chemically distinct blocks that have been connected with a covalent bond (*14*). Microphase separation produces morphologies largely set by the volume fraction, such as lamellae, cylinders, or spheres. Although these fundamental morphologies have been well studied for decades, the factors that determine the range of orientational and translational order (grain size) are not well understood. The coarsening kinetics in three dimensions have been studied (*15–17*), but no mechanistic understanding of the ordering process has been developed, partly owing to lack of data on the real-space dynamics during pattern development, which is our focus here.

A polystyrene-polyisoprene (PS-PI) diblock was synthesized by means of living anionic polymerization with masses of 30 and 11 kg/mol for the PS and PI blocks (SI 30-11) to produce PI cylinders in a PS matrix. This diblock was applied to carbon-coated silicon substrates by spin coating from a dilute solution, and order was induced through vacuum annealing (Fig. 1A) (*18*). A representative image from a similar system shows cylinders (lighter) lying parallel to the substrate (Fig. 1B). Because samples sizes were on the order of square centimeters, there were at least 10^5 microdomain repeat spacings in any direction, thereby negating edge effects. After annealing, microdomains were preferentially stained with the vapors of OsO_4 to provide contrast for a Zeiss 982 scanning electron microscope (SEM) (*18–20*). The SEM allowed us to image large areas of the polymer film at high resolution for accurate measurements of the average grain size.

The orientational correlation length (ξ_2) of the pattern was measured as a function of annealing time to quantitatively characterize the degree of microdomain order. This was accomplished by collecting many SEM images of each sample and computationally measuring the local orientational order parameter, $\psi(\vec{r}) = \exp[2i\theta(\vec{r})]$, where $\vec{r}$ is position and θ is the microdomain or stripe orientation (similar to director) (*21*). The azimuthally averaged correlation function $g_2(r) = \langle\psi(0)\psi(r)\rangle$ was then calculated and the correlation length ξ_2 was measured by fitting $g_2(r)$ with e^{-r/ξ_2}. Two annealing temperatures (413 K and 443 K) were examined

[1]Department of Physics, [2]Princeton Materials Institute, [3]Department of Chemical Engineering, Princeton University, Princeton, NJ 08544, USA. [4]Jet Propulsion Laboratory, 4800 Oak Grove Drive, Mailstop 302-306, Pasadena, CA 91109, USA.

*Present address: ExxonMobil Research and Engineering Company, 1545 Route 22 East, Annandale, NJ 08801–0998, USA.